Multiple Small Scale Landslides Triggered by Typhoon Talas 2011

Ryo Okuwaki[1,2], Wenyuan Fan[3], Masumi Yamada[4], Hikaru Osawa[1], Tim J. Wright[2]

[1] *Mountain Science Center, Faculty of Life and Environmental Sciences, University of Tsukuba, Tsukuba, Ibaraki 305-8572, Japan*
[2] *COMET, School of Earth and Environment, University of Leeds, Leeds LS2 9JT, UK*
[3] *Scripps Institution of Oceanography, UC San Diego, La Jolla, California 92093, USA*
[4] *Disaster Prevention Research Institute, Kyoto University, Uji, Kyoto 611-0011, Japan*

Key Points:

- Multiple typhoon-triggered landslides were newly identified by using a novel surface-wave detector
- Small 100-m-scale landslide effectively radiated coherent surface waves propagating up to 3,000 km
- Small and large landslides may follow the same empirical scaling relationship

*Corresponding author
rokuwaki@geol.tsukuba.ac.jp (Ryo Okuwaki)

Abstract

Landslides can cause devastating damage. In particular, heavy rainfall-triggered landslides pose a chain of natural hazards. However, such events are often difficult to detect, leaving the physical processes poorly understood. Here we apply a novel surface-wave detector to detect and locate landslides during the transit of Typhoon Talas 2011. We identify multiple landslides triggered by Typhoon Talas, including a landslide in the Tenryu Ward, Shizuoka, Japan, ~400 km east from the typhoon track. The Tenryu landslide displaced a total mass of 3.1×10^9 kg, which is much smaller than typical surface wave detected landslides, yet generated coherent seismic signals propagating up to 3,000 km away. Our observations demonstrate that typhoons can cause heavy rainfall in distant regions to trigger landslides far away from their tracks. Our results also suggest an alerting technology to detect and locate landslides with a sparse seismic network.

Plain Language Summary

Landslides can reshape the Earth surface. Occasionally, landslides are triggered by strong tropical cyclones (typhoons). Typhoons cause heavy rainfall during their transits, and the rainwater infiltrates into the ground and raises the groundwater table. These physical processes can facilitate gravitational stresses to exceed the resistive strength of the material and trigger landslides. Heavy rainfall-triggered landslides may further cause debris flow and initiate a chain of catastrophic hazards. Thus it is critical to know how often landslides are triggered by heavy rainfall and what physical mechanisms are modulating such triggering processes. Here, by using a novel seismic surface wave detector, we find that Typhoon Talas triggered multiple landslides, including a landslide in the Tenryu region that was 400 km away from the typhoon-transit track. These landslides occurred during the typhoon passage through western Japan, September 3–4, 2011. Our results suggest an effective monitoring approach of landslides that can robustly detect and locate remote landslides with a sparse seismic network, and our method can be potentially implemented in near-real time.

1. Introduction

Landslides can deform in a wide range of spectrum from aseismically to seismically. These slope failure events can displace mass over a large range of volumes and last from seconds to years (Ekström and Stark, 2013, Delbridge *et al.*, 2016, Hu *et al.*, 2020). Such mass wasting events can cause significant hazards to mountain communities and infrastructure (e.g., Spiker and Gori, 2003). In particular, deep-seated landslides that move rapidly with a large volume of deposits are catastrophic (Hewitt *et al.*, 2008, Chigira *et al.*, 2013). Mitigations of such disastrous events rely on robust monitoring of landslide failure processes, yet observations of landslide dynamics remain rare. Broadband seismic observations can help detecting and locating these events even when landslides are distant from the seismic networks (Ekström and Stark, 2013, Fan *et al.*, 2020).

Landslides can generate broadband seismic signals (Allstadt, 2013, Hibert *et al.*, 2015). Short-periods (< 1 s) (Yamada *et al.*, 2012, Doi and Maeda, 2020) and intermediate- to long-periods (30 to 150 s) (Ekström and Stark, 2013, Allstadt, 2013, Li *et al.*, 2019, Zhang *et al.*, 2019) seismic signals are commonly used for detecting landslides and studying landslide dynamics. For example, short-period signals have proven efficient for detecting and evaluating landslides in Taiwan and other regions (Dietze *et al.*, 2017, Fuchs *et al.*, 2018, Dammeier *et al.*, 2016, Manconi *et al.*, 2016, Chao *et al.*, 2017). Such operations are often limited to local or regional distances due the attenuation of short-period seismic signals. The intermediate- to long-period (35 to 150 s) seismic surface waves are the primary means to detect and locate distant landslides (Ekström, 2006, Ekström and Stark, 2013). For example, Rayleigh waves have proven effective for detecting teleseismic landslides (Ekström, 2006, Lin *et al.*, 2010). These landslides can displace $\geq 2\times10^{10}$ kg rocks and generate surface waves with amplitudes equivalent to those of magnitude $M \geq 4.6$ earthquakes (Ekström, 2006, Ekström and Stark, 2013). However, smaller size landslides are infrequently reported from surface wave detectors, leaving their occurrence poorly understood.

Heavy rain from tropical cyclones can trigger landslides, and such combined hazards in conjunction with possible debris flow and flooding can greatly amplify regional hazard intensities (Kuo *et al.*, 2018, Hung *et al.*, 2019, Lin *et al.*, 2008, Saito *et al.*, 2010, Tsou *et al.*, 2011, Chigira *et al.*, 2013). For example, increasing river flow due to a typhoon in combination with internal erosion of dams can lead to failures of landslide-dammed lakes, which can cause debris flow further downstream (Schneider *et al.*, 2013). Mechanically, heavy rainfalls from tropical cyclones can facilitate gravitational stresses to exceed the resistive strength of the material by increasing pore-pressure and reducing friction on the failure plane (Iverson, 2000, Schulz *et al.*, 2009). A prominent example is the 2011 Typhoon Talas, which brought precipitation exceeding 2,000 mm and caused 50+ landslides adjacent to the typhoon track in Nara, Wakayama and Mie prefectures in western Japan (Yamada *et al.*, 2012, Chigira *et al.*, 2013). Intriguingly, it also caused 1,000+ mm precipitation in Shizuoka prefecture, ~400 km away from the typhoon track (Fig. 1b). However, no landslides were reported in this region by previous seismic studies (e.g., Yamada *et al.*, 2012).

Here we apply a surface-wave detector that is based on the AELUMA method (Automated Event Location Using a Mesh of Arrays) (de Groot-Hedlin and Hedlin, 2015, Fan *et al.*, 2018) to investigate landslide activities across Japan during the transit of Typhoon Talas. Our approach has been successfully applied to the USArray with over 400 stations and located various unconventional seismic sources (Fan *et al.*, 2018, 2019, 2020). We identify three new landslides, including one in Tenryu, Shizuoka prefecture, which is 400 km away from the track of Typhoon Talas. The landslide generates coherent surface wavefields that are recorded by stations across Japan and Taiwan but only displace a total mass of 3.1×10^9 kg. The results show promises of our method in near-real-time monitoring of landslide activities in Japan.

2. Data and Method

We use continuous seismic data from 103 stations of the National Research Institute for Earth Science and Disaster Resilience F-net (NIED, 2019) and the Broadband Array in Taiwan for Seismology TW (IES, 1996) networks. We download the vertical-component long-period (1-s-sampled LHZ) records of September 3–4, 2011, during Typhoon Talas' transit in Japan (Fig. 1, Yamada *et al.*, 2012). We then remove the instrumental response to utilize data from different instruments. The records are bandpass filtered at 20 to 50 s with a 4th-order non-causal Butterworth filter.

Following (de Groot-Hedlin and Hedlin, 2015), we first divide the 103 stations into non-overlapping 68 triangular subarrays (triads), and remove triads with internal angles beyond the range of 30° to 120° (Fig. 1a) (Lee and Schachter, 1980, Thompson and Shure, 2016). For each triad, we measure relative travel times between station pairs of coherent signals to solve for a centroid arrival time and a propagation direction. We then invert the seismic source locations with aggregations of the measurements by grid-searching possible source locations (Fan *et al.*, 2018). To neutralize off-great-circle path propagation effects, we also apply empirical calibrations from measurements of earthquakes in the Global Centroid Moment Tensor (GCMT) project (Dziewonski *et al.*, 1981, Ekström *et al.*, 2012) and landslides reported in a previous study (Yamada *et al.*, 2012). After obtaining the source locations, we perform a quality control step to discard sources detected by less than 10 triads. These empirical parameters are different than those applied to the USArray (e.g., Fan *et al.*, 2018), but comparable parameters were examined in (de Groot-Hedlin and Hedlin, 2018) and proven effective. Details of the algorithm are described in (Fan *et al.*, 2018) and (de Groot-Hedlin and Hedlin, 2015).

In total, we locate 25 seismic sources from September 3 to 4, 2011. We further screen the sources by visually inspecting the waveform records aligned with the source epicenters, and 16 candidate sources generating coherent wave trains are kept for further evaluations (e.g., Fig. 2a). Thirteen of the candidate sources are earthquakes in standard earthquake catalogs (Dziewonski *et al.*, 1981, Ekström *et al.*, 2012, Japan Meteorological Agency, 2011, U.S. Geological Survey Earthquake Hazards Program, 2017) and two sources are landslides reported in (Yamada *et al.*, 2012). We find one new unknown seismic source (Fig. 2).

To investigate the source mechanism, we examine near-source station records filtered in multiple frequency bands and find that the signals are clearly visible in a narrow intermediate period band (20 to 50 s) but do not show clear *P*- or *S*-arrivals (Figs. S2 and S3). As discussed later, the seismic source is likely a landslide, and we follow previous studies to model the source as centroid-single forces (CSF) (Kawakatsu, 1989, Tsai and Ekström, 2007, Ekström and Stark, 2013). Here we use a conventional time-

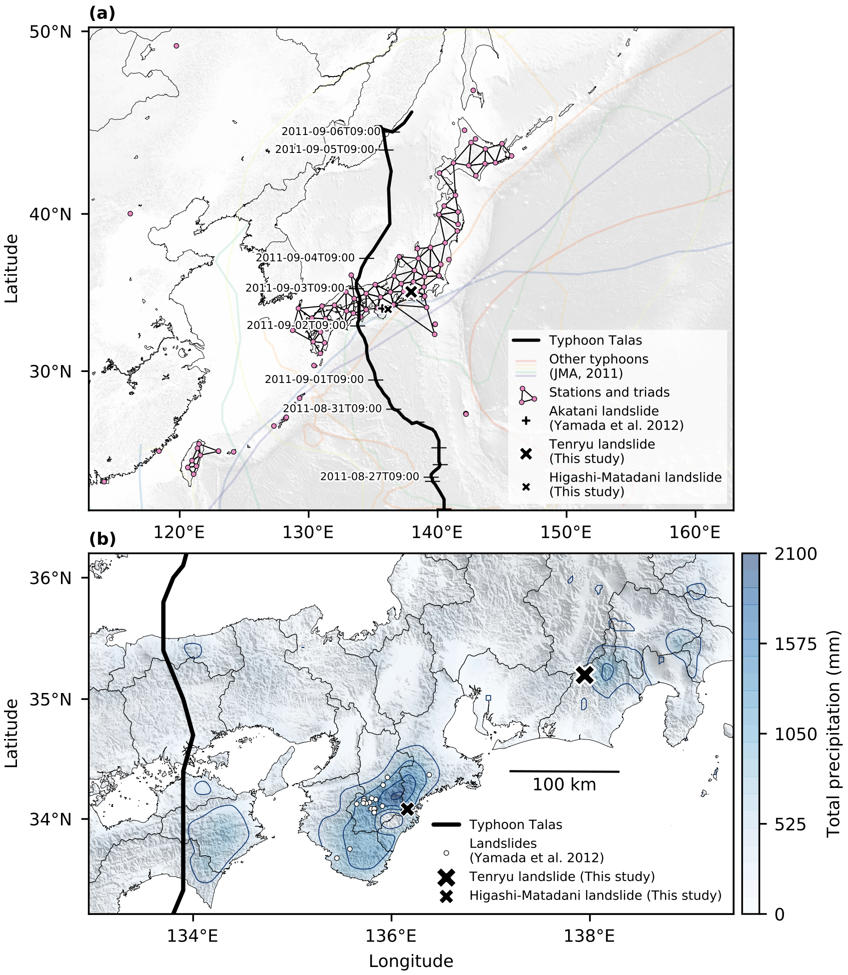

Figure 1: Overview of the study area. (a) Map shows the available seismic stations during the study period, the track of Typhoon Talas, and the landslide locations. Background topography/bathymetry are from the GEBCO 2019 Grid (GEBCO Bathymetric Compilation Group 2019, 2019). (b) Background color is the total precipitation during August 30, 2011 to September 6, 2011 observed at the Automated Meteorological Data Acquisition System (AMeDAS) stations. The blue contour denotes every 500 mm total precipitation. The gray lines denote the administrative boundaries.

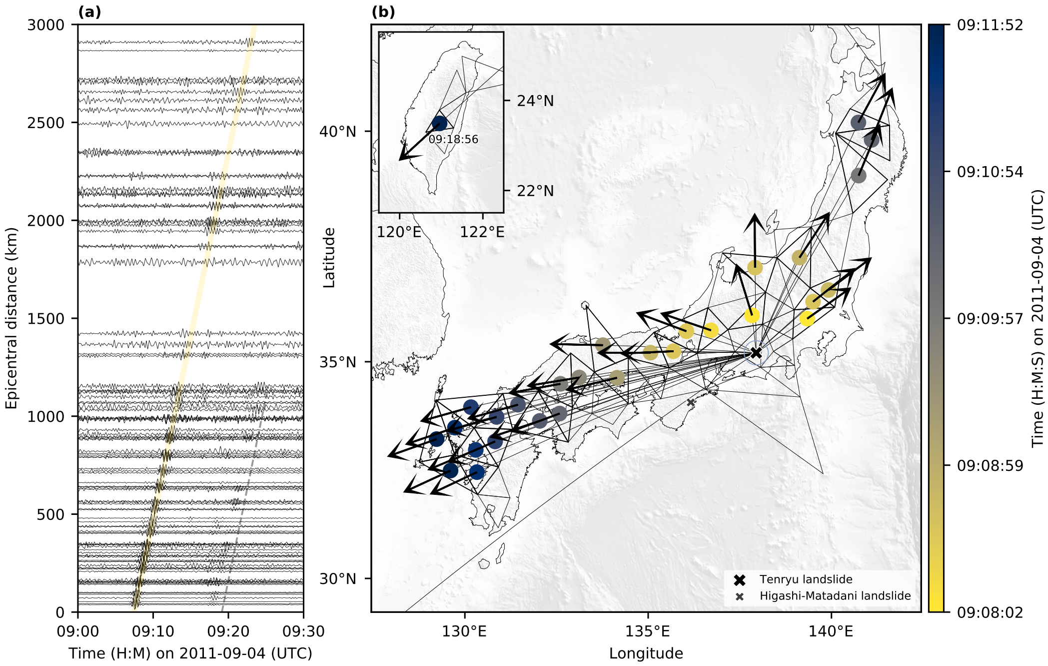

Figure 2: Detection and location of the Tenryu landslide. (a) Self-normalized bandpass-filtered (20 to 50 s) waveforms aligned by the epicenter of the Tenryu landslide. The yellow line shows the reference wavefront travelling at a phase velocity of 3.11 km/s. The dashed line indicates wavetrains travelled from the Higashi-Matadani landslide. (b) The thick and thin triangles are the triad subarrays. The arrow is the observed arrival angle. The color for each dot represents the observed arrival time. The thin line between the epicenter and the centroid of each triad is the great circle path. The blue ellipse denotes the estimated location uncertainty. The large and small cross markers are the epicenters of the Tenryu and Higashi-Matadani landslides. Inset is the measurement in Taiwan for the Tenryu landslide.

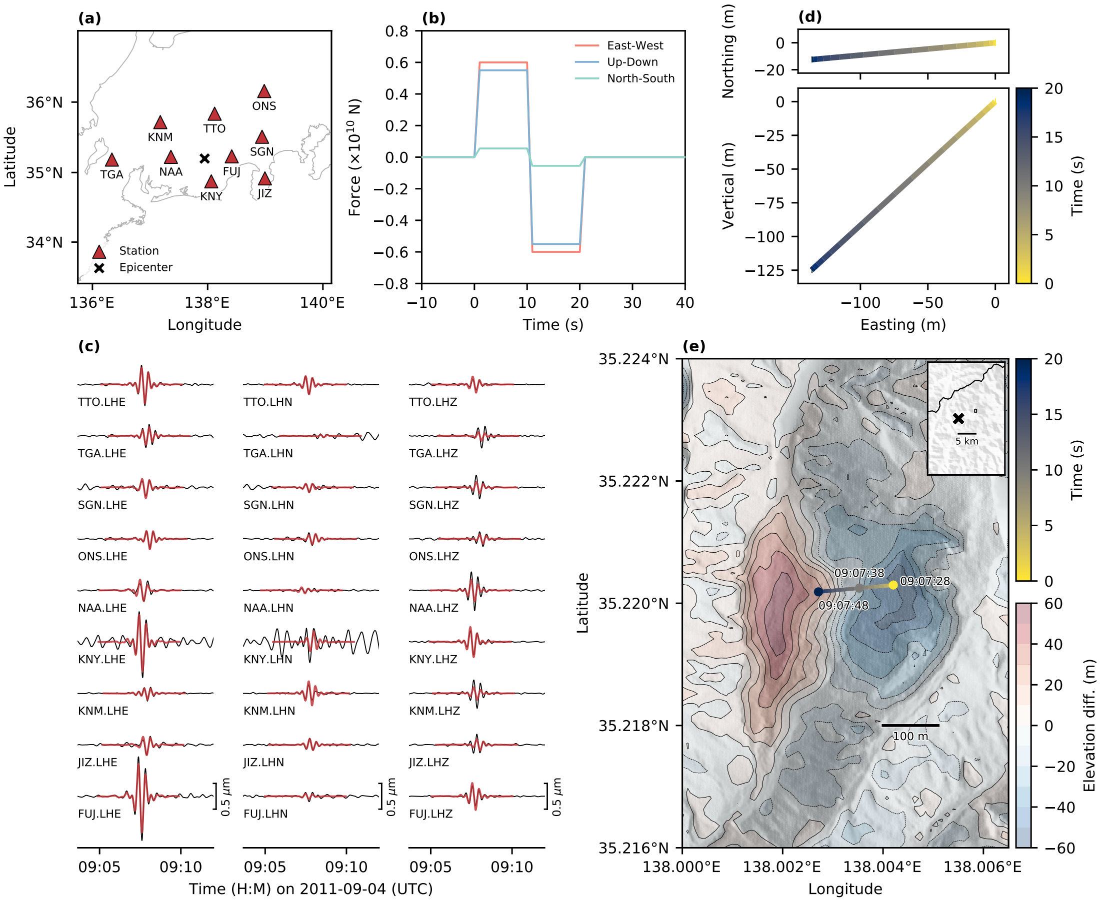

Figure 3: Summary of the centroid single force (CSF) modelling and the digital elevation models (DEMs) of the Tenryu landslide. (a) Distribution of the stations used for the CSF modelling. (b) The inverted three-component force-time function. (c) Black and red lines are the observed and synthetic waveforms, which are bandpass filtered at 20 to 50 s. Station codes and channels are listed on each column. (d) East-North and East-Vertical trajectories (displacements) of the center of mass. Color represents the time. (e) Colored contour denotes the differentiation of DEMs before and after the landslide. Colored line is the trajectory of the center of mass, along with the time on September 4, 2011 (UTC). The inset is the regional map. The small rectangle is the area of Fig. 3e. The black line denotes the administrative boundary.

domain method to obtain a CSF model by grid-searching the force duration and the three-component centroid force amplitudes (Fan *et al.*, 2020). Our model can explain 20-to-50-s Rayleigh and Love waves at 9 nearfield stations (Fig. 3a). Details are documented in the Supporting Information (Text S1).

3. Results

We locate an unknown seismic source on September 4, 2011, 09:07:28 (UTC) in Tenryu Ward, Shizuoka Prefecture, Japan (35.1992°N, 137.9479°E, Fig. 2b). The waveform record-section shows a coherent wavefield propagating up to 3,000 km with an estimated phase velocity of 3.11 km/s (Fig. 2a). The location is obtained with 29 triads, including one in Taiwan (2,000 km away from the epicenter) (Fig. 2b). The location uncertainty is ~30 km (Fig. 2b), which is about one grid separation (~30 km) (Fan *et al.*, 2018). The surface-wave magnitude (M_{SW}) (Ekström, 2006) of the event is 4.3. Our preferred CSF model of the Tenryu event has a misfit reduction of 72% and has peak force amplitudes of 0.55×10^{10} N, 0.055×10^{10} N, and 0.6×10^{10} N for the up-down, north-south, and east-west components, respectively (Fig. 3b). We obtain a source duration of 20 s albeit the boxcar model being less sensitive to the force duration (Tsai and Ekström, 2007). Sharp increase in the data misfit for models of longer durations suggests that the Tenryu event evolved rapidly (Table S1).

We also observe a peculiar coherent phase ~10 min after the Tenryu event (Fig. 2a). We re-examine the propagation direction and centroid time measurements and locate a source with only 7 triads. This source is located near Higashi-Matadani in Mie prefecture (34.0823°N, 136.1602°E), occurring on 09:16:58 (UTC), September 4, 2011 (Fig. S5b) with a location uncertainty of ~30 km. This event is adjacent to the Ohtaki landslide identified in (Yamada *et al.*, 2012) but occurred one hour later than the Ohtaki landslide. There was a Japan Meteorological Agency (JMA) magnitude (M_{JMA}) 1.7 earthquake in the area, but the near-field short-period records show that the event was not the M_{JMA} 1.7 earthquake (Fig. S4). The detected event was likely a new unknown seismic source (e.g., Yamada *et al.*, 2012). We perform a similar CSF modeling to investigate the Higashi-Matadani event and find that the event can be well explained as centroid single forces (Fig. S6). The estimated duration was 24 seconds and the maximum centroid force was estimated as 0.34×10^{10} N. Furthermore, we identify another coherent phase ~3.5 min before the signals associated with the Higashi-Matadani event (Fig. S5a). The amplitude of these signals is about 50% of those of the Higashi-Matadani event and the signal was about 30 seconds long. Our surface wave detector can not locate this seismic source due to the poor signal-to-noise ratios. However, this event is likely to be close to the Higashi-Matadani event because the near-field stations observe almost equal separation times between the two phases (Figs. S2 and S4). We will discuss the source of this signal in the next section.

4. Discussion and Conclusions

Our detected seismic sources are unlikely to be typical earthquakes. The seismic sources generated signals that are distinctly different from those of regular earthquakes. For regular earthquakes, e.g., a moment magnitude (M_{W}) 5.1 earthquake (with the source duration ~1 s), seismic waveforms have clear P- and S-wave arrivals, and both short-period ground motions can be identified up to 300 km away (Fig. S7c). However, the short-period ground motions of the newly identified seismic sources dissipate significantly at a similar distance range (Fig. S7b). Strong dissipation of short-period signals makes it difficult to locate these sources with standard techniques (Figs. S4 and S7b). In contrast, we observe clear and coherent intermediate-period (20 to 50 s) surface waves at stations up to 3,000 km away (Figs. 2a and S5a). These abnormal seismic radiations clearly differ from those of typical earthquakes.

Our detected seismic source in Tenryu Ward, Shizuoka city is likely to be a landslide identified by the local forest office in Shizuoka prefecture. This landslide was reported 3 days after the event time and is within 5 km of our detected seismic source (Fig. 3e). The landslide was further confirmed by the aerial photos from the Geospatial Information Authority of Japan (GSI) (Geospatial Information Authority of Japan, 2011b) and can be clearly identified in the optical satellite imageries (Fig. S10). The field survey used a Laser Profiler to construct a digital elevation model (DEM). By differencing the DEMs before and after the landslide, the elevation changes show that the mass slid 200–250 m along the slope from east to west with a width range of ~300 m (Fig. 3e). The DEM model suggests that the Tenryu landslide displaced a total volume of 1.2–1.5×10^6 m^3, covering a region of $\sim 9.0 \times 10^4$ m^2 with a maximum thickness of ~50 m (Fig. 3e) (Kanto Regional Forest Office Japan, 2012, Seo *et al.*, 2012, Yumoto and Takashima, 2013). Assuming an average density of 2.6×10^3 kg/m^3, the landslide displaced a total mass of 3.1–3.9×10^9 kg.

Our preferred CSF model of the Tenryu landslide has the maximum centroid force (F_{max}) of 0.82×10^{10} N, suggesting a total displaced mass of 4.4×10^9 kg if we assume an empirical scaling relationship (Ekström and Stark, 2013). To understand the landslide dynamics, we explore the CSF model uncertainties by examining an ensemble of models that can explain the observations within 5% of the minimum misfit (≤ 0.296) (Table. S1, Fig. S11). This exercise suggests that the F_{max} is likely within $0.77 \pm 0.06 \times 10^{10}$ N, indicating that the displaced mass ranges from 3.8–4.5×10^9 kg. The seismically inferred total mass agrees with the field survey estimate, despite that the empirical scaling relationship was drawn from landslides ten times larger than the Tenryu event (Fig. 4a). For example, the Siachen landslides in the high mountains of Pakistani Kashmir deposited mass complexes on the order of 0.188×10^{12} kg and generated centroid forces on the order of 10^{11} N (Ekström and Stark, 2013). Further, the seismically inferred maximum momentum and the M_{SW} magnitude fit the scaling relationships as well (Ekström and Stark, 2013) (Fig. 4c). These agreements validate the scaling relationships over a large range of landslide sizes (Ekström and Stark, 2013).

With the seismically determined mass, we can further obtain the sliding acceleration history and the failure trajectory from the CSF model by double integrating the acceleration functions (Fig. 3d). The failure trajectory suggests that the mass slid 136 m horizontally towards the west and 125 m downward, a runout distance of 185 m. This displacement estimate agrees well with the ground truth observation (Fig. 3e). The results show promises of obtaining accurate landslide trajectories in remote regions where satellite images or field surveys are limited. We also estimate the dynamic frictional coefficient μ with a total mass of 3.1×10^9 kg (Text S2, Brodsky *et al.*, 2003, Yamada *et al.*, 2013), which ranges from 0.23 to 0.46 with respect to a slope of 25° to 38° (Text S2 and Fig. S8), concurring with μ of documented major landslides ($0.2 \leq \mu \leq 0.6$, e.g., Mt. St. Helens, Brodsky *et al.*, 2003). Our results show that seismic modeling efforts can reveal details of landslide failure processes and they agree well with ground truth observations.

However, the relationship between the runout duration and the potential energy loss of the Tenryu landslide differ from those of other catastrophic landslides in (Ekström and Stark, 2013) (Fig. 4b). This is likely because the vertical displacement is comparable to the runout length of the Tenryu landslide, in contrast to landslides dominated by horizontal movements in other regions (Fig. 4d). The Tenryu landslide occurred within a narrow valley and displaced along a steep slope, which is underlain by the alternated layers of sandstone and mudstone (Fig. 3e) (Kanto Regional Forest Office Japan, 2012, Yumoto and Takashima, 2013). The layers are part of the Late Cretaceous accretionary-sedimentary rocks that develop fragile textures involving fractures and joints (Kanto Regional Forest Office Japan, 2012). Similar geological predispositions of deep-seated landslides are also found in the southwest direction on the ridgeline of the landslide (Fig. 3e). High erosion rate due to the extreme climate and active tectonic regime may have facilitated the development of high-relief mountains and steep hills

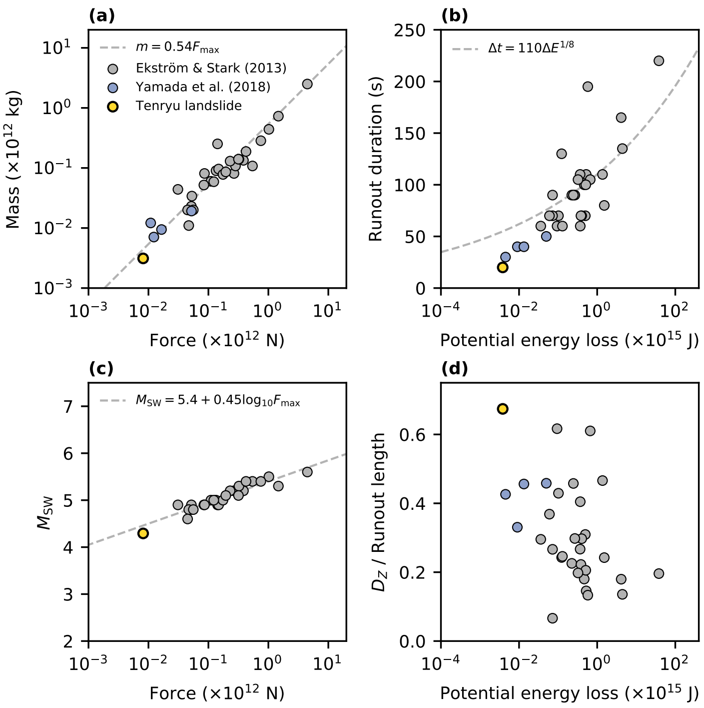

Figure 4: Scatter plot of landslide parameters. (a) Maximum centroid force (F_{max}) versus landslide mass. The Tenryu landslide mass in this study is from field observations. (b) Potential energy loss versus runout duration. (c) F_{max} versus surface wave magnitude (M_{SW}). (d) Potential energy loss versus the ratio of the vertical mass-center displacement (D_Z) and runout length. The runout length corresponds to the summation of the East-West, North-South, Up-Down displacement vectors from the CSF modelling.

across the Japanese island, which likely causes landslides in the region with short durations and large vertical displacements (Yamada *et al.*, 2018, Oguchi *et al.*, 2001).

In addition to the Tenryu landslide, we also find two events near Higashi-Matadani in Mie prefecture, where many deep-seated landslides were reported from field surveys after the typhoon transit. The first source is likely the Higashi-Matadani landslide, corresponding to the largest field-reported landslide (Sakai, 2011, Numamoto *et al.*, 2012). Based on the differential DEMs (Geospatial Information Authority of Japan, 2011a), the elevation change shows the mass moved from south-east to north-west (Fig. S9). Following a similar scaling exercise (Ekström and Stark, 2013), we estimate the mass of the Higashi-Matadani event as 1.8×10^9 kg and the volume as 7.0×10^5 m^3 from the resolved CSF model, assuming a density of 2.6×10^3 kg/m^3 (Yamada *et al.*, 2013). The CSF model shows the mass displaced from south-east to north-west, matching well with the topography change measured by the DEMs (Fig. S9a). The other source occurs ~3.5 min before the Higashi-Matadani landslide, but is challenging to locate with the current dataset. This event is likely the Mochiyama-Tanigawa landslide, which is located about 1 km north-west of Higashi-Matadani landslide (Sakai, 2011, Numamoto *et al.*, 2012). The surface area of this landslide is about 30% of the Higashi-Matadani landslide. However, the occurrence time reported by local residents is 40 mins before our detection time (Numamoto *et al.*, 2012). The timing inconsistency undermines the landslide hypothesis. However, no coherent seismic phases were recorded 40 mins before the Higashi-Matadani landslide. Alternatively, the smaller signal may be associated with a precursory event of the Higashi-Matadani landslide.

The Tenryu landslide is ∼400 km east from the track of Typhoon Talas, where large precipitations from the typhoon were observed. Investigating such hazards away from the track requires a robust detection method that can effectively monitor a broad region. Our results suggest a useful detection algorithm that can identify small (∼100 m scale) landslides with a sparse network in addition to dense continental scale arrays, e.g. USArray (Fan *et al.*, 2020). The success shows promises to implement the technique to study environmental processes in regions that are less well instrumented. Our approach is effective because it does not require phase-picking, prior knowledge of source type, or an accurate velocity model to calculate travel times. Our approach uses local coherence across a triad, which helps remove strong path effects of seismic wave propagation and hence is effective to detect remote landslides. Although ground, aerial, and satellite methods can be used to map landslides with high spatial resolution, it is worth mentioning that it took 3 days for the local agencies to identify and survey the Tenryu landslide (Yumoto and Takashima, 2013). These methods are often hampered by poor weather, restricting access and satellite visibility (e.g., Razak *et al.*, 2013). Our seismic method can resolve landslide locations and times in near-real time and may be helpful for future risk management and rapid response of post-event surveys.

Acknowledgments

The authors would like to thank the editor Jeroen Ritsema, the associate editor Victor Tsai, the reviewer Goran Ekström, and the anonymous reviewer for their handing and constructive suggestions, which have led to improvements of the paper. The authors thank NIED and IRIS for making the data publicly available. The facilities of IRIS Data Services, and specifically the IRIS Data Management Center, were used for access to waveforms, related metadata, and/or derived products used in this study. IRIS Data Services are funded through the Seismological Facilities for the Advancement of Geoscience (SAGE) Award of the National Science Foundation under Cooperative Support Agreement EAR-1851048. This work has been supported by Grant-in-Aid for JSPS Fellows JP19J00814 (R.O.) and JSPS Grant-in-Aid for Early-Career Scientists JP17H04733 (M.Y.) and JP20K14570 (R.O.). W.F. acknowledges support from National Science Foundation grants OCE-1833279 and OPP-1838464. The authors thank Haoran Meng, Xinyu Luo, Taka'aki Taira, Shunsuke Takemura, and Takahiko Uchide for fruitful discussion.

Data Availability Statement

Waveform data at F-net (https://doi.org/10.17598/nied.0005) and Hi-net (https://doi.org/10.17598/nied.0003) are available through NIED website (https://hinetwww11.bosai.go.jp/auth/download/cont/?LANG=en). The facilities of IRIS Data Services and specifically the IRIS DMC (https://ds.iris.edu/ds/nodes/dmc/) are used for access to waveforms and related metadata. AELUMA MATLAB code bundle is available from IRIS DMC (https://ds.iris.edu/ds/products/infrasound-aeluma/). Green's functions used for the CSF modeling are provided by Data Services Products: Synthetics Engine (https://doi.org/10.17611/DP/SYNGINE.1). The typhoon tracks are downloaded at https://www.data.jma.

go.jp/fcd/yoho/typhoon/route_map/index.html. The AMeDAS precipitation data are downloaded at https://www.data.jma.go.jp/gmd/risk/obsdl/index.php. The DEM data are available at https://fgd.gsi.go.jp/download/menu.php. ObsPy (Beyreuther *et al.*, 2010, version 1.1.0; https://doi.org/10.5281/zenodo.165135), matplotlib (Hunter, 2007, version 3.0.3; https://doi.org/10.5281/zenodo.2577644), and the Generic Mapping Tools (Wessel and Luis, 2017, version 6.1; http://doi.org/10.5281/zenodo.3924517) were used to generate figures. The CVX package (Grant and Boyd, 2008, 2014, http://cvxr.com/cvx; http://stanford.edu/~boyd/graph_dcp.html) was used for solving the least-square problem in locating source. The DEM data after the Tenryu landslide was provided by Chubu Regional Development Bureau, Ministry of Land, Infrastructure, Transport and Tourism, Japan. The DEM data of the Higashi-Matadani landslide was provided by the Geospatial Information Authority of Japan.

References

Allstadt, K., 2013. Extracting source characteristics and dynamics of the August 2010 Mount Meager landslide from broadband seismograms, *J. Geophys. Res. Earth Surf.*, **118**(3), 1472–1490, doi: 10.1002/jgrf.20110.

Beyreuther, M., Barsch, R., Krischer, L., Megies, T., Behr, Y., and Wassermann, J., 2010. ObsPy: A Python Toolbox for Seismology, *Seismol. Res. Lett.*, **81**(3), 530–533, doi: 10.1785/gssrl.81.3.530.

Brodsky, E. E., Gordeev, E., and Kanamori, H., 2003. Landslide basal friction as measured by seismic waves, *Geophys. Res. Lett.*, **30**(24), 1–5, doi: 10.1029/2003GL018485.

Chao, W.-A., Wu, Y.-M., Zhao, L., Chen, H., Chen, Y.-G., Chang, J.-M., and Lin, C.-M., 2017. A first near real-time seismology-based landquake monitoring system, *Sci. Rep.*, **7**(1), 43510, doi: 10.1038/srep43510.

Chigira, M., Tsou, C.-Y., Matsushi, Y., Hiraishi, N., and Matsuzawa, M., 2013. Topographic precursors and geological structures of deep-seated catastrophic landslides caused by Typhoon Talas, *Geomorphology*, **201**, 479–493, doi: 10.1016/j.geomorph.2013.07.020.

Dammeier, F., Moore, J. R., Hammer, C., Haslinger, F., and Loew, S., 2016. Automatic detection of alpine rockslides in continuous seismic data using hidden Markov models, *J. Geophys. Res. Earth Surf.*, **121**(2), 351–371, doi: 10.1002/2015JF003647.

de Groot-Hedlin, C. D. and Hedlin, M. A., 2015. A method for detecting and locating geophysical events using groups of arrays, *Geophys. J. Int.*, **203**(2), 960–971, doi: 10.1093/gji/ggv345.

de Groot-Hedlin, C. D. and Hedlin, M. A. H., 2018. A New Automated Approach to Detecting and Locating Seismic Events Using Data from a Large Network, *Bull. Seismol. Soc. Am.*, **108**(4), 2032–2045, doi: 10.1785/0120180072.

Delbridge, B. G., Bürgmann, R., Fielding, E., Hensley, S., and Schulz, W. H., 2016. Three-dimensional surface deformation derived from airborne interferometric UAVSAR: Application to the Slumgullion Landslide, *J. Geophys. Res. Solid Earth*, **121**(5), 3951–3977, doi: 10.1002/2015JB012559.

Dietze, M., Mohadjer, S., Turowski, J. M., Ehlers, T. A., and Hovius, N., 2017. Seismic monitoring of small alpine rockfalls – validity, precision and limitations, *Earth Surf. Dyn.*, **5**(4), 653–668, doi: 10.5194/esurf-5-653-2017.

Doi, I. and Maeda, T., 2020. Landslide Characteristics Revealed by High-Frequency Seismic Waves from the 2017 Landslide in Central Japan, *Seismol. Res. Lett.*, doi: 10.1785/0220200032.

Dziewonski, A. M., Chou, T.-A., and Woodhouse, J. H., 1981. Determination of earthquake source parameters from waveform data for studies of global and regional seismicity, *J. Geophys. Res. Solid Earth*, **86**(B4), 2825–2852, doi: 10.1029/JB086iB04p02825.

Ekström, G., 2006. Global Detection and Location of Seismic Sources by Using Surface Waves, *Bull. Seismol. Soc. Am.*, **96**(4A), 1201–1212, doi: 10.1785/0120050175.

Ekström, G. and Stark, C. P., 2013. Simple Scaling of Catastrophic Landslide Dynamics, *Science (80-.).*, **339**(6126), 1416–1419, doi: 10.1126/science.1232887.

Ekström, G., Nettles, M., and Dziewoński, A., 2012. The global CMT project 2004–2010: Centroid-moment tensors for 13,017 earthquakes, *Phys. Earth Planet. Inter.*, **200-201**, 1–9, doi: 10.1016/j.pepi.2012.04.002.

Fan, W., de Groot-Hedlin, C. D., Hedlin, M. A. H., and Ma, Z., 2018. Using surface waves recorded by a large mesh of three-element arrays to detect and locate disparate seismic sources, *Geophys. J. Int.*, **215**(2), 942–958, doi: 10.1093/gji/ggy316.

Fan, W., McGuire, J. J., Groot-Hedlin, C. D., Hedlin, M. A. H., Coats, S., and Fiedler, J. W., 2019. Stormquakes, *Geophys. Res. Lett.*, **46**(22), 12909–12918, doi: 10.1029/2019GL084217.

Fan, W., McGuire, J. J., and Shearer, P. M., 2020. Abundant Spontaneous and Dynamically Triggered Submarine Landslides in the Gulf of Mexico, *Geophys. Res. Lett.*, **47**(12), 1–16, doi: 10.1029/2020GL087213.

Fuchs, F., Lenhardt, W., and Bokelmann, G., 2018. Seismic detection of rockslides at regional scale: examples from the Eastern Alps and feasibility of kurtosis-based event location, *Earth Surf. Dyn.*, **6**(4), 955–970, doi: 10.5194/esurf-6-955-2018.

GEBCO Bathymetric Compilation Group 2019, 2019. The GEBCO_2019 Grid - a continuous terrain model of the global oceans and land, doi: https://doi.org/10/c33m.

Geospatial Information Authority of Japan, 2011a. Fundamental Geospatial Data, Retrieved from: https://fgd.gsi.go.jp/download/menu.php.

Geospatial Information Authority of Japan, 2011b. Aerial photos of the Tenryu landslide, Retrieved from: https://saigai.gsi.go.jp/2011typhoon12/html/112.html.

Grant, M. and Boyd, S., 2008. Graph implementations for nonsmooth convex programs, in *Recent Adv. Learn. Control*, Lecture Notes in Control and Information Sciences, pp. 95–110, eds Blondel, V., Boyd, S., and Kimura, H., Springer-Verlag Limited, Retrieved from: http://stanford.edu/~boyd/graph_dcp.html.

Grant, M. and Boyd, S., 2014. CVX: Matlab Software for Disciplined Convex Programming, version 2.1, Retrieved from: http://cvxr.com/cvx.

Hewitt, K., Clague, J. J., and Orwin, J. F., 2008. Legacies of catastrophic rock slope failures in mountain landscapes, *Earth-Science Rev.*, **87**(1-2), 1–38, doi: 10.1016/j.earscirev.2007.10.002.

Hibert, C., Stark, C. P., and Ekström, G., 2015. Dynamics of the Oso-Steelhead landslide from broadband seismic analysis, *Nat. Hazards Earth Syst. Sci.*, **15**(6), 1265–1273, doi: 10.5194/nhess-15-1265-2015.

Hu, X., Bürgmann, R., Schulz, W. H., and Fielding, E. J., 2020. Four-dimensional surface motions of the Slumgullion landslide and quantification of hydrometeorological forcing, *Nat. Commun.*, **11**(1), 2792, doi: 10.1038/s41467-020-16617-7.

Hung, C., Lin, G.-W., Leshchinsky, B., and Kuo, H.-L., 2019. Extracting region-specific runout behavior and rainfall thresholds for massive landslides using seismic records: a case study in southern Taiwan, *Bull. Eng. Geol. Environ.*, **78**(6), 4095–4105, doi: 10.1007/s10064-018-1384-5.

Hunter, J. D., 2007. Matplotlib: A 2D Graphics Environment, *Comput. Sci. Eng.*, **9**(3), 90–95, doi: 10.1109/MCSE.2007.55.

IES, 1996. Broadband Array in Taiwan for Seismology, doi: 10.7914/SN/TW.

Iverson, R. M., 2000. Landslide triggering by rain infiltration, *Water Resour. Res.*, **36**(7), 1897–1910, doi: 10.1029/2000WR900090.

Japan Meteorological Agency, 2011. The Seismological Bulletin of Japan.

Kanto Regional Forest Office Japan, 2012. Report: Disaster investigation of the 2011 Misakubo landslide, Tech. rep.

Kawakatsu, H., 1989. Centroid single force inversion of seismic waves generated by landslides, *J. Geophys. Res.*, **94**(B9), 12363, doi: 10.1029/JB094iB09p12363.

Kuo, H.-L., Lin, G.-W., Chen, C.-W., Saito, H., Lin, C.-W., Chen, H., and Chao, W.-A., 2018. Evaluating critical rainfall conditions for large-scale landslides by detecting event times from seismic records, *Nat. Hazards Earth Syst. Sci.*, **18**(11), 2877–2891, doi: 10.5194/nhess-18-2877-2018.

Lee, D. T. and Schachter, B. J., 1980. Two algorithms for constructing a Delaunay triangulation, *Int. J. Comput. Inf. Sci.*, **9**(3), 219–242, doi: 10.1007/BF00977785.

Li, W., Chen, Y., Liu, F., Yang, H., Liu, J., and Fu, B., 2019. Chain-Style Landslide Hazardous Process: Constraints From Seismic Signals Analysis of the 2017 Xinmo Landslide, SW China, *J. Geophys. Res. Solid Earth*, **124**(2), 2025–2037, doi: 10.1029/2018JB016433.

Lin, C. H., Kumagai, H., Ando, M., and Shin, T. C., 2010. Detection of landslides and submarine slumps using broadband seismic networks, *Geophys. Res. Lett.*, **37**(22), n/a–n/a, doi: 10.1029/2010GL044685.

Lin, G.-W., Chen, H., Hovius, N., Horng, M.-J., Dadson, S., Meunier, P., and Lines, M., 2008. Effects of earthquake and cyclone sequencing on landsliding and fluvial sediment transfer in a mountain catchment, *Earth Surf. Process. Landforms*, **33**(9), 1354–1373, doi: 10.1002/esp.1716.

Manconi, A., Picozzi, M., Coviello, V., De Santis, F., and Elia, L., 2016. Real-time detection, location, and characterization of rockslides using broadband regional seismic networks, *Geophys. Res. Lett.*, **43**(13), 6960–6967, doi: 10.1002/2016GL069572.

NIED, 2019. NIED F-net, doi: 10.17598/nied.0005.

Numamoto, S., Takezawa, N., Ito, H., Matsuoka, A., and Hayashi, S., 2012. Deep-seated collapses and sediment transport caused by Typhoon No. 12 at Odaicho in Mie Prefecture in 2011, in *Abstr. Annu. Conf. Japan Soc. Eros. Control Eng.*, Retrieved from: http://www.jsece.or.jp/event/conf/abstract/2012/pdf/Pb-33.pdf.

Oguchi, T., Saito, K., Kadomura, H., and Grossman, M., 2001. Fluvial geomorphology and paleohydrology in Japan, *Geomorphology*, **39**(1-2), 3–19, doi: 10.1016/S0169-555X(01)00048-4.

Razak, K. A., Santangelo, M., Van Westen, C. J., Straatsma, M. W., and de Jong, S. M., 2013. Generating an optimal DTM from airborne laser scanning data for landslide mapping in a tropical forest environment, *Geomorphology*, **190**, 112–125, doi: 10.1016/j.geomorph.2013.02.021.

Saito, H., Nakayama, D., and Matsuyama, H., 2010. Relationship between the initiation of a shallow landslide and rainfall intensity—duration thresholds in Japan, *Geomorphology*, **118**(1-2), 167–175, doi: 10.1016/j.geomorph.2009.12.016.

Sakai, T., 2011. Report on the Joint Field Survey of Disasters in Mie Prefecture Caused by Typhoon No. 12 in 2011 by Japanese Geotechnical Society and Chubu Geological Survey Association, Tech. rep., Retrieved from: https://www.jiban.or.jp/file/file/mie1006.pdf.

Schneider, J. F., Gruber, F. E., and Mergili, M., 2013. Recent Cases and Geomorphic Evidence of Landslide-Dammed Lakes and Related Hazards in the Mountains of Central Asia, in *Landslide Sci. Pract.*, vol. 6, pp. 57–64, Springer Berlin Heidelberg, Berlin, Heidelberg, doi: 10.1007/978-3-642-31319-6_9.

Schulz, W. H., Kean, J. W., and Wang, G., 2009. Landslide movement in southwest Colorado triggered by atmospheric tides, *Nat. Geosci.*, **2**(12), 863–866, doi: 10.1038/ngeo659.

Seo, N., Tsuchiya, S., Osaka, O., Takashima, M., and Asami, K., 2012. Large-scale collapse and landslide dam in a national forest in Mizukubo Town, Hamamatsu City, due to heavy rains by Typhoon No.12 (2011), in *Abstr. Annu. Conf. Japan Soc. Eros. Control Eng.*, Retrieved from: http://www.jsece.or.jp/event/conf/abstract/2012/pdf/T1-04.pdf.

Spiker, E. C. and Gori, P. L., 2003. National landslide hazards mitigation strategy : a framework for loss reduction, Tech. rep., doi: 10.3133/cir1244.

Thompson, C. M. and Shure, L., 2016. *Image Processing Toolbox: For Use with MATLAB;[user's Guide]*, MathWorks.

Tsai, V. C. and Ekström, G., 2007. Analysis of glacial earthquakes, *J. Geophys. Res.*, **112**(F3), F03S22, doi: 10.1029/2006JF000596.

Tsou, C.-Y., Feng, Z.-Y., and Chigira, M., 2011. Catastrophic landslide induced by Typhoon Morakot, Shiaolin, Taiwan, *Geomorphology*, **127**(3-4), 166–178, doi: 10.1016/j.geomorph.2010.12.013.

U.S. Geological Survey Earthquake Hazards Program, 2017. Advanced National Seismic System (ANSS) Comprehensive Catalog of Earthquake Events and Products, doi: 10.5066/F7MS3QZH.

Wessel, P. and Luis, J. F., 2017. The GMT/MATLAB Toolbox, *Geochemistry, Geophys. Geosystems*, **18**(2), 811–823, doi: 10.1002/2016GC006723.

Yamada, M., Matsushi, Y., Chigira, M., and Mori, J., 2012. Seismic recordings of landslides caused by Typhoon Talas (2011), Japan, *Geophys. Res. Lett.*, **39**(13), 1–5, doi: 10.1029/2012GL052174.

Yamada, M., Kumagai, H., Matsushi, Y., and Matsuzawa, T., 2013. Dynamic landslide processes revealed by broadband seismic records, *Geophys. Res. Lett.*, **40**(12), 2998–3002, doi: 10.1002/grl.50437.

Yamada, M., Mangeney, A., Matsushi, Y., and Matsuzawa, T., 2018. Estimation of dynamic friction and movement history of large landslides, *Landslides*, **15**(10), 1963–1974, doi: 10.1007/s10346-018-1002-4.

Yumoto, H. and Takashima, M., 2013. Investigation and analysis of the landslide dam in Mizukubo town, in *Publ. Collect. For. For. Technol. Kanto Reg. For. Off.*, pp. 69–73, Retrieved from: https://jglobal.jst.go.jp/en/detail?JGLOBAL_ID=201302252352901877&rel=0.

Zhang, Z., He, S., Liu, W., Liang, H., Yan, S., Deng, Y., Bai, X., and Chen, Z., 2019. Source characteristics and dynamics of the October 2018 Baige landslide revealed by broadband seismograms, *Landslides*, **16**(4), 777–785, doi: 10.1007/s10346-019-01145-3.